NSRRC - Journal (2014)

Journal of Materials Chemistry A

ROYAL SOCIETY OF CHEMISTRY

PAPER

View Article Online
View Journal | View Issue

Published on 03 June 2014. Downloaded by National Tsing Hua University on 11/09/2014 09:34:43.

CrossMark click for updates

Cite this: J. Mater. Chem. A, 2014, 2, 12991

Multiscale structure of calcium- and magnesium-silicate-hydrate gels†

W.-S. Chiang,[a] G. Ferraro,[b] E. Fratini,[b] F. Ridi,[b] Y.-Q. Yeh,[c] U-S. Jeng,[c] S.-H. Chen*[a] and P. Baglioni*[b]

Received 17th March 2014
Accepted 30th May 2014

DOI: 10.1039/c4ta02479f

www.rsc.org/MaterialsA

Concrete is the world's most widely used building material. However, the production of CaO-based cements generates large amounts of anthropogenic emissions of CO_2. Among different strategies to reduce CO_2 emissions, newly developed MgO-based cements, though currently suffering from inferior mechanical properties, are some of the most promising and attractive options. By combining wide- and small-angle X-ray scattering and electron microscopy, we identified differences in the multiscale structure of the two main binding phases: the calcium-silicate-hydrate (C-S-H) gel for CaO-based cements and the magnesium-silicate-hydrate (M-S-H) gel for MgO-based cements. We found the primary unit at the nanoscale level of C-S-H to be a multilayer disk-like globule, whereas for M-S-H it is a spherical globule. These prominent differences result in diverse microstructures, leading to disparities in mechanical properties and durability for the associated cements. Modulating the M-S-H structure and enhancing the compatibility between C-S-H and M-S-H will be the key to improve the robustness of eco-friendly MgO-based binders.

1. Introduction

Although concrete is one of the most used construction materials by mankind (≈10 km^3 per year), the manufacture of cement, *i.e.* its main binder, currently contributes more than 5% to all human-generated greenhouse-gas release.[1,2] In this context, one of the main challenges in the cement industry is to develop alternatives which have similar mechanical properties but generate less CO_2 emissions.[3]

Recently, strong attention has been focused on hydraulic binders based on highly reactive periclase (MgO). This oxide reacts with water and a silica source forming an amorphous solid phase, magnesium-silicate-hydrate ($(MgO)_x$–SiO_2–$(H_2O)_y$ abbreviated as M-S-H),[4] responsible for the structural arrest of the hydrated matrix ("setting" of cement). This phase is analogous to calcium-silicate-hydrate ($(CaO)_x$–SiO_2–$(H_2O)_y$ abbreviated as C-S-H), which is colloidal in nature[5,6] and is the main hydration product and a primary binding phase in Portland cement.[7] MgO-based cements[8–11] can be obtained by partially or fully using magnesium silicates, which replace the carbon-rich limestone originally required in the CaO-based Portland Cement (PC) production process.[7] Therefore, the production process of MgO-based cements involves low or even negative CO_2 emissions if part of the MgO reacts with CO_2. Using magnesium silicates as raw materials to produce large amounts of MgO is a realistic approach since they are very abundant on a global basis (magnesium orthosilicate constitutes about 70% of the Earth's mantle).[12] Even though MgO-based cements have the potential to transform a production route with one of the highest environmental impacts to an eco-friendly process,[13] their large-scale usage is mainly limited by their inferior mechanical properties.[10,11] For example, it is known that the mechanical response of MgO-based cements or MgO–PC blends is usually inferior to that of PC alone[11] if not carbonated in special ways.[14,15]

It has been demonstrated that understanding and predicting the macro-scale mechanical properties of materials necessarily require a deep knowledge of their microstructure;[16] as a matter of fact, cement compressive strength can be empirically expressed as a function of the microstructure (*i.e.* porosity).[17] Since M-S-H and C-S-H gels are mainly amorphous, small-angle scattering techniques are particularly well-suited for the determination of their microstructure.[18] Previous investigations by small-angle X-ray[19–23] and neutron[24–28] scattering (SAXS and SANS) characterized the morphology of the C-S-H gel at the nanoscale, highlighting the surface and mass fractal nature of the hydrated pastes. Recently, SANS contrast variation experiments determined the mean chemical formula, $(CaO)_{1.7}$-$SiO_2(H_2O)_{1.8}$, and mass density, 2.604 Mg m^{-3}, of C-S-H particles in hydrated cement pastes.[29] In addition, the combination

[a]Department of Nuclear Science and Engineering, Massachusetts Institute of Technology, Cambridge, MA, USA. E-mail: sowhsin@mit.edu

[b]Department of Chemistry "Ugo Schiff" and CSGI, University of Florence, via della Lastruccia 3-Sesto Fiorentino, I-50019, Florence, Italy. E-mail: piero.baglioni@unifi.it

[c]National Synchrotron Radiation Research Center, Hsinchu Science Park, Hsinchu 30076, Taiwan

† Electronic supplementary information (ESI) available. See DOI: 10.1039/c4ta02479f

Published on 03 June 2014. Downloaded by National Tsing Hua University on 11/09/2014 09:34:43.

of SAXS, SANS and ^{29}Si-NMR techniques refined the structure of the primary particle (globule) in synthetic pure C-S-H phases[30] as well as in C-S-H gels containing structurally defined comb-shaped superplasticizers as additives.[31,32]

In this study, we investigated the differences in the morphology and microstructure between synthetic M-S-H,[33] C-S-H,[34] and their 1 : 1 mixture. The C-S-H/M-S-H blend was investigated to understand the compatibility of the two hydrates at the nano- and micro-scale level. We also explored the effect of the Ca/Si ratio and the influence of cellulose ether on the microstructure of C-S-H. By combining wide- and small-angle X-ray scattering and electron microscopy, we disclosed the multiscale structure of M-S-H, C-S-H, and the mixed gels from angstrom to micrometer length-scale. Significant differences emerged between the microstructures, shedding light on the origin of the diverse mechanical properties among the MgO- and CaO-based cements and opening a way to develop sustainable and eco-friendly binders.

2. Results and discussion

2.1 Nanometer to submicron length-scale

The SAXS data and the corresponding fitting curves for the (a) C-S-H and (b) M-S-H and Mixed gels are shown in Fig. 1. The parameters used for the data fitting of all the investigated gels are listed in Table 1. The description of the different samples and the details of the SAXS analytical models applied in the fitting procedures are described in the Experimental section and ESI.†

Fig. 1a shows that the SAXS data of C-S-H gels can be fitted very well across 3 orders of magnitude in the scattering vector range (2.3×10^{-3} Å^{-1} < Q < 0.74 Å^{-1}) using a model of polydisperse multilayer disk-like globules packing into a fractal structure. This is consistent with previous studies by some of the authors.[30,31]

The data analysis results presented in Table 1 underline that the size of C-S-H disks can be tuned by controlling the Ca/Si ratio. Comparing CSH-A (Ca/Si = 1) with CSH-B (Ca/Si = 1.4), it is evident that the increasing Ca/Si ratio reduces the effective size of the globules (R_e ~68 Å for CSH-A and R_e ~26 Å for CSH-B as indicated in Table 1). The radius of the disk R becomes much smaller although the average number of layers $\bar{n}$ becomes slightly larger in CSH-B. Moreover, the calcium silicate thickness (L_2) becomes larger but the interlayer distance (L) turns out to be smaller when increasing the Ca/Si ratio. A similar decrease in the interplanar distance of C-S-H with the increase in the Ca/Si ratio was also highlighted in a recent study.[35] Furthermore, He *et al.*[36] studied the morphology of the C-S-H gels prepared by the hydrothermal route at 95 °C with different Ca/Si ratios using scanning electron microscopy (SEM). They found that a gel with a lower Ca/Si ratio (Ca/Si = 1) exhibits a sheet shape, while C-S-H with a higher Ca/Si ratio (Ca/Si > 1.3) displays a fibrillar morphology at the microscale level. The much smaller disk radius R found in CSH-B (Ca/Si = 1.4) may possibly explain why in the sample with high Ca/Si ratio it is hard for the globules to pack into a more planar and continuous morphology at a larger length-scale. It should be noted that SEM and SAXS probe the microstructure of the gels in different size domains. The larger detectable size achieved in the present SAXS experiment (~100 nm) is a tenth of the scale-bar of the SEM images studied by He *et al.*[36]

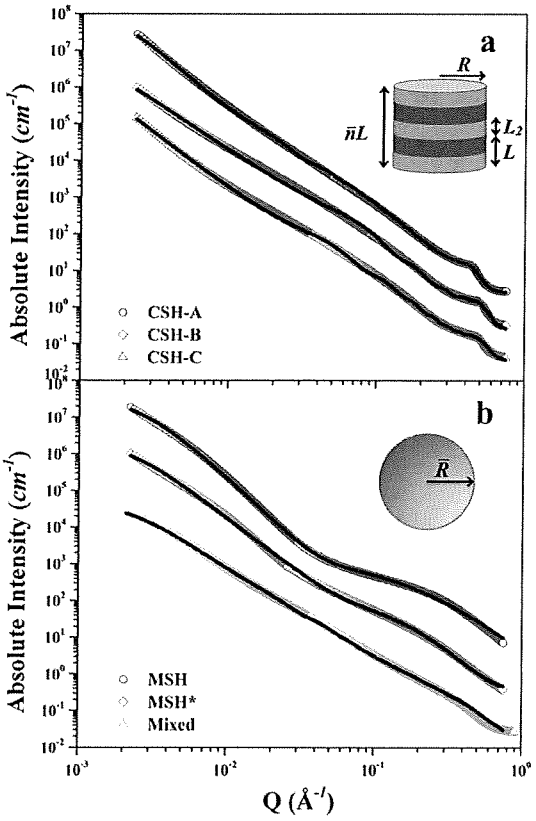

Fig. 1 Model fitting results of SAXS data for (a) C-S-H and (b) M-S-H and mixed samples. Panel (a) shows the experimental data for CSH-A (blue open circle), CSH-B (olive open diamond), and CSH-C (red open up-triangle). Panel (b) shows the experimental data for MSH (violet open circle), MSH* (pink open diamond), and mixed (orange open up-triangle). The corresponding data fitting curves are all denoted by black lines. The experimental and fitting intensities are shifted on the y-axis for the sake of clarity. The error bars of the experimental data represent one standard deviation and are smaller than the symbols. The geometrical models used in the case of C-S-H and M-S-H globules are also highlighted.

The globule structure and morphology of the C-S-H gel can also be tuned by using different types of additives.[31] In order to address this point, a C-S-H gel was grown in the presence of methylhydroxyethyl cellulose (Culminal), an additive commonly employed by the cement industry. Table 1 shows that Culminal additive favours the formation of small C-S-H globules as compared to the pure gel at the same Ca/Si ratio (*i.e.* CSH-A *versus* CSH-C). The interaction of a cellulose derivative with C-S-H primary units results in a significant reduction in the disk radius and a slight decrease of the average number of layers inside the globules. The interlayer distance L also becomes smaller while the thickness of the calcium silicate layer L_2 is not changed. According to the literature,[37] cellulose ethers facilitate the extrusion of cement paste. Together with the viscosity

 This journal is © The Royal Society of Chemistry 2014

Published on 03 June 2014. Downloaded by National Tsing Hua University on 11/09/2014 09:34:43.

Table 1 Parameters extracted from the model fitting of SAXS data of C-S-H, M-S-H and C-S-H/M-S-H mixed samples[a]

Sample	D	ξ (Å)	R (Å)	L (Å)	L_2 (Å)	$\bar{n}$	Z_n	χ	R_e (Å)
CSH-A	2.881(1)	752.6(1)	128.468(2)	14.251(1)	5.752(2)	1.790(1)	0.206(1)	0.001(lb)	68.096(5)
CSH-B	2.530(1)	1327(1)	30.837(1)	12.364(1)	7.319(3)	1.930(1)	1.308(1)	0.001(lb)	25.724(1)
CSH-C	2.757(1)	3000(ub)	49.612(1)	12.598(1)	5.908(2)	1.509(1)	0.521(1)	0.079(1)	32.742(3)
Mixed	2.608(1)	403.5(2)	[b]	13.85(1)	[b]	[b]	[b]	[b]	[b]
	D	ξ (Å)	$\bar{R}$ (Å)				Z_R		
MSH	2.971(1)	374.38(2)	17.414(1)	—	—	—	2.232(1)	—	—
MSH*	2.753(1)	443.46(2)	16.482(1)	—	—	—	4.879(1)	—	—
Mixed	3(ub)	28.86(5)	[b]	—	—	—	[b]		
	N_{CSH}	N_{MSH}							
Mixed	365.6(2)	2.614(1)						—	—

[a] lb (or ub) means the fitting value collapses onto the lower (or upper) boundary limit. The values in the parenthesis are one standard deviation from the nonlinear least-squares fitting process. [b] Other structural parameters of Mixed shown in eqn (4) are fixed to the same values of CSH-A and MSH.

modifying effect of the additive polymers, the higher mobility of the globules due to the reduced globule size can contribute to explain this effect induced by the cellulose derivative.

In addition, SEM images (see Fig. 4) indicate that the foil-like morphology becomes less extended when adding Culminal.

Since the building blocks pack into a fractal structure, the size, shape, and the polydispersity of the globules will definitely affect the resulting fractal arrangement described by mass fractal dimension, D and fractal cutoff, ξ. The large disk radius R of CSH-A suggests that in this case the microstructure of the C-S-H gel is more like a continuous structure with planar pores as proposed by McDonald *et al.*[38] This continuous and extended planar structure can explain the higher fractal dimension obtained in CSH-A. The increase of the Ca/Si ratio and the inclusion of Culminal in the C-S-H gel both have the effect of reducing the extension of the planar structure and consequently achieve a more open arrangement (a smaller D). Moreover, the analysis of SAXS data shows that increasing the Ca/Si ratio or adding Culminal can enlarge the "fractal domain" (increase ξ, see Table 1).

Fig. 2a shows the Schultz distribution of the total thickness $t = nL$ of the multilayer disk-like globules in CSH-A, CSH-B, and CSH-C. The small Z_n (Table 1, upper part) found in all cases indicates that the globules are very polydisperse. The averages of the total thickness $\bar{t} = \bar{n}L$ are 25.5 Å, 23.9 Å, and 19.0 Å and the standard deviations of the total thickness $\sigma_t = \bar{n}L/(Z_n+1)^{1/2}$ are 23.2 Å, 15.7 Å, and 15.4 Å for CSH-A, CSH-B, and CSH-C, respectively. Overall these results show the possibility to control the size, shape, and polydispersity of the constituent globules and therefore to tune the macroscopic properties of PC.

Fig. 1b shows the SAXS data and the corresponding fitting curves for the M-S-H samples (MSH and MSH*) and the mixed C-S-H/M-S-H sample (Mixed). The fitting parameters used in Fig. 1b are listed in the lower part of Table 1. In the case of the M-S-H gel, the multilayer disk model gives unphysical results (see Table S1 in the ESI†). The absence of the high-Q peak corresponding to the multilayer sub-structure indicated that the

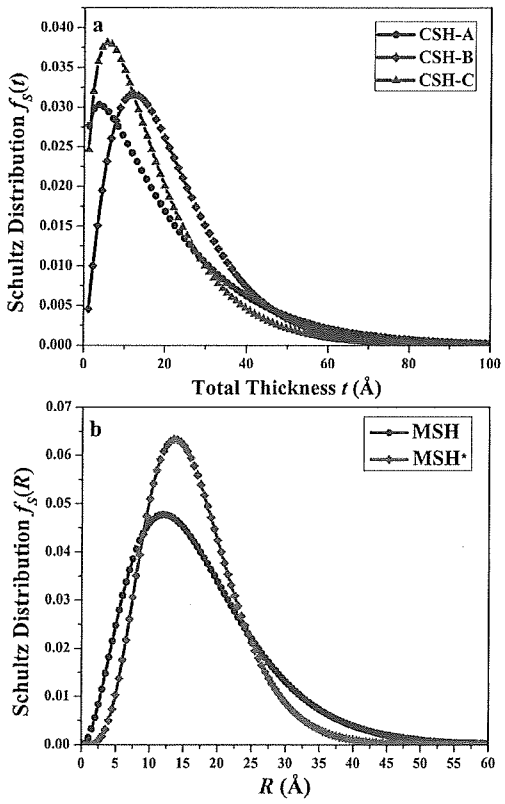

Fig. 2 (a) The effective Schultz distribution of the total thickness $t = nL$ of the multilayer disk-like globules, due to the distribution of the number of repeating layers n, for CSH-A (blue solid circle), CSH-B (olive solid diamond), and CSH-C (red solid up-triangle). We assume that no distribution of the disk radius R of the globules occurs. (b) The Schultz distribution of the radius R of the spherical globules for MSH (violet solid circle) and MSH* (pink solid diamond). The normalization conditions are $\int_0^\infty f_S(t)\,dt = 1$ and $\int_0^\infty f_S(R)\,dR = 1$.

Published on 03 June 2014. Downloaded by National Tsing Hua University on 11/09/2014 09:34:43.

C-S-H model is not appropriate to be applied to M-S-H samples. For these reasons, we used a model of polydisperse spheres arranged into a fractal structure. The match between the data and fitting curves for both MSH and MSH* over the wide Q range indicates that this simpler model works very well for these samples. The structural difference of the basic building blocks can account for the totally different mechanical properties of CaO-based and MgO-based cements. The binding force between disk-like globules in C-S-H is stronger than that between spherical globules in M-S-H because in the first case surface contacts dominate, while in the second case only point-like contacts are predominant.

Table 1 (lower part) evidences that the average radius $\bar{R}$ of the spherical globules is about the same for MSH and MSH* ($\bar{R} \sim 17$ Å). However, the size distribution of the globules is wider in MSH. This can be seen from the Schultz distribution of the radius R shown in Fig. 2b. The standard deviations of the radius distribution $\sigma_R = \bar{R}/(Z_R + 1)^{1/2}$ are 9.7 Å and 6.8 Å for MSH and MSH*, respectively. In addition, the larger fractal dimension D for MSH indicates that the globules arrange more compactly in the fractal structure as compared to the MSH* case. Masoero *et al.*[39] also found an increase in packing density with polydispersity in cements composed of spherical building particles. Interestingly, the fractal cutoff ξ found in M-S-H samples is much smaller than that found in C-S-H gels. This suggests that in M-S-H the fractal structure expands less in space than in C-S-H. The much larger fractal size found in C-S-H indicates a stronger binding force between the globules to maintain and expand a larger fractal domain. The fractal dimensions of CSH-A and MSH are both very large, implying that compact fractal structures can be achieved by double-decomposition in solutions. However, D is higher in the MSH case. This is in full agreement with the fact that it is easier to pack spheres into compact structures than disks. Cho *et al.*[40] studied the effect of the particle shape on the packing density in natural and crushed sands. They found that irregularity (*i.e.* decreasing the sphericity or roundness of the particles) can hinder the particle mobility and therefore make the particles hard to arrange themselves into a dense packing configurations. Although the particles they investigated are much bigger in size than the globules we studied here, the basic packing mechanism should be similar.

As shown in Fig. 1, a peak indicative of a layered structure is still evident in the mixed sample even though it is broader than that in the pure C-S-H. In addition, the peak for the mixed sample is superposed by a broad shoulder characteristic of polydisperse spheres. We therefore fitted the SAXS curve of the mixed sample by a linear combination of the curves of the pristine CSH-A and MSH gels, which were synthesized using the same chemical route, assuming that the interaction between the C-S-H and M-S-H fractals is negligible (see eqn (4)). We only allowed the change of pre-factors N_{CSH} and N_{MSH} and fractal parameters D_{CSH}, ξ_{CSH}, D_{MSH}, and ξ_{MSH}. The interlayer distance L_{CSH} was set as a variable to account for the slight change of the peak position, however it does not change much compared with the CSH-A case (see Table 1). Fig. 1b shows the high agreement between SAXS data and the corresponding fitting curve based on this combined model. The results show that the fractal dimension D of both C-S-H and M-S-H components does not change much in the mixed sample compared with the pure counterparts, CSH-A and MSH. Nevertheless, the fractal cutoff ξ of both components decreases significantly. The result suggests that both kinds of globules pack into similar fractals as in the pure cases whereas the fractal domains become much smaller when the gel contains equal amounts of Ca and Mg. The decrease in the correlation length of the fractal arrangement in the presence of M-S-H is clear evidence of the disrupting effect imposed by this phase to the C-S-H gel.

2.2 Angstrom length-scale

Fig. 3 shows the wide-angle X-ray scattering (WAXS) data for all the six samples. There are sharp peaks in WAXS patterns for CSH-A, CSH-B, and CSH-C located at $Q = 2.05$ Å^{-1} and 2.23 Å^{-1} characteristic of tobermorite $Ca_5(Si_6O_{16}(OH)_2)\cdot 4(H_2O)$ (see ref. 36 and references therein), indicating the formation of a quite ordered structure at the angstrom level. In contrast, the broad bumps of MSH and MSH* centred at $Q = 1.84$ Å^{-1} and 2.45 Å^{-1} suggest that lizardite[43] may form in M-S-H gels although the phases present are mostly amorphous in nature. WAXS patterns indicate that Brucite, $Mg(OH)_2$, is not present in MSH and MSH* because of the absence of its characteristic peaks.[11] The WAXS data for the mixed sample contain features of both C-S-H and M-S-H components as the pattern is the superposition of C-S-H sharp peaks and M-S-H broad shoulders.

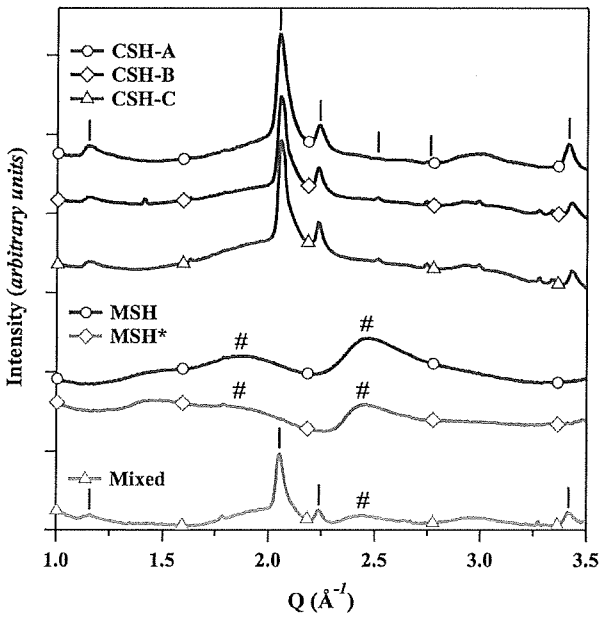

Fig. 3 WAXS data for CSH-A (blue, open circle), CSH-B (olive, open diamond), CSH-C (red, open up-triangle), MSH (violet, open circle), MSH* (pink, open diamond), and mixed (orange, open up-triangle). "|" indicates the peaks attributed to tobermorite $Ca_5(Si_6O_{16}(OH)_2)\cdot 4(H_2O)$[38] and "#" denotes the peaks attributed to lizardite $(Mg_3Si_2O_5(OH)_4)$.[41] The WAXS intensities are shifted along the y-axis for the sake of clarity.

 This journal is © The Royal Society of Chemistry 2014

Published on 03 June 2014. Downloaded by National Tsing Hua University on 11/09/2014 09:34:43.

2.3 Submicron to micrometer length-scale

Fig. 4 shows the morphology of all the six hydrated phases investigated by SEM. CSH-A exhibits leafy or sheet-shape objects arranging in a dense, laminar pattern in agreement with previous work.[36]

CSH-B with a target ratio of Ca/Si = 1.4 is similar in morphology to CSH-A; however the foils are more polydisperse and tiny fibrils coexist. CSH-C, which is the C-S-H gel prepared in the presence of Culminal, has a different morphology from the other two C-S-H samples; in particular, the foil-like morphology is less extended. The SEM image of MSH shown in Fig. 4d evidences an irregular porosity between interconnected and densely packed spherical particles (diameter between 30 and 50 nm) at the submicron level. On the other hand, in MSH* (see Fig. 4e) there are both small and large spherical particles, indicating a higher polydispersity as a result of the direct reaction of solids (silica fume and CaO). It seems that the difference in structure between the basic building blocks of C-S-H and M-S-H reflects disparity in morphology at a larger length-scale. All the C-S-H cases exhibit a laminar pattern while the M-S-H cases show the morphology of connected spheres at the submicron to micrometer length-scale. The extended structure of C-S-H suggests stronger binding force and better mechanical properties because the foil-like objects in C-S-H have more extended surface contact than the spherical particles found in the M-S-H gel. Finally, the mixed sample (see Fig. 4f) presents regions of a typical M-S-H structure alternating with regions of a characteristic C-S-H morphology. The presence of these mixed features is in agreement with the WAXS and SAXS results (see Fig. 3 and 1b) and with previously reported experiments. Co-precipitated M-S-H and C-S-H are essentially immiscible as a result of intrinsic structural differences between the two hydrated phases from angstrom to micrometer length-scale.

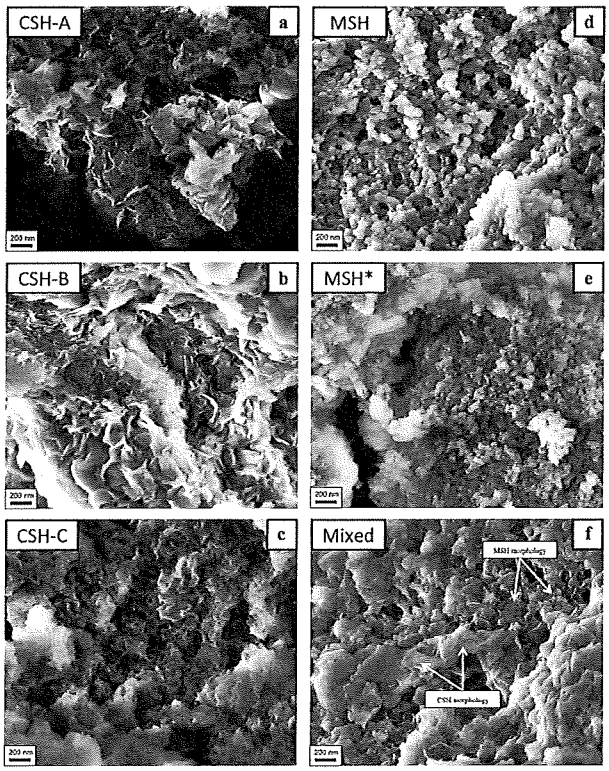

Fig. 4 SEM micrographs of: (a) CSH-A, (b) CSH-B, (c) CSH-C, (d) MSH, (e) MSH*, and (f) mixed samples at a magnification of 90k×. Scale bar is 200 nm.

3. Experimental

3.1 Sample preparation

A pure M-S-H gel (sample MSH) with a Mg/Si ratio equal to 1 was prepared through double-decomposition synthesis according to the method described by Brew and Glasser.[33] Stock solutions of sodium metasilicate ($Na_2SiO_3 \cdot 4H_2O$) and magnesium nitrate ($Mg(NO_3)_2 \cdot 6H_2O$) were prepared. Both solutions were cooled to about 0 °C. The magnesium solution was slowly added to sodium silicate under stirring in a two-necked round-bottomed flask. The flask was kept in an ice-water bath under continuous N_2 flux. The product was warmed to ambient temperature and the precipitate settled readily, leaving a clear supernatant solution. In order to remove residual sodium, the precipitate was washed (diafiltrated) with deionized water under a N_2 atmosphere (to avoid carbonation). At the end of the process, a small fraction of the supernatant was analysed for Na^+ concentration using flame atomic absorption spectroscopy ($[Na^+] < 0.20 \pm 0.01$ ppm) to ensure that the by-product $NaNO_3$ was completely removed by the washing procedure. The same procedure was used to synthesize C-S-H with a Ca/Si ratio equal to 1 (sample CSH-A) and 1.4 (sample CSH-B) using calcium nitrate instead of magnesium nitrate. The mixed C-S-H/M-S-H gel (sample mixed) was synthesized using calcium and magnesium nitrate in order to have a Ca/Mg ratio equal to 1. In addition, we synthesized a sample (sample CSH-C) of C-S-H (Ca/Si = 1) containing methylhydroxyethyl cellulose (commercial name Culminal) as an additive (2.4% w/w respect to the amount of solid phase). The M-S-H gel was also synthesized starting from highly reactive solid MgO and silica fume (SF) according to Cheeseman *et al.*[10] (sample MSH*). A paste of 30 wt% MgO and 70 wt% SF with a water-to-solid ratio of 3 was prepared by adding a mixture of the solids to water and mixing the paste for 15 min. This alternative method to synthesize M-S-H is very similar to the real hydration process taking place in MgO-based cement pastes. For clarity, Table S0 (see ESI†) summarizes the preparation methods and the characteristics of the investigated samples. The elemental compositions of the samples were measured using energy-dispersive X-ray analysis (EDX) and are listed in Table S4 (see ESI†).

3.2 Small-angle X-ray scattering (SAXS) and wide-angle X-ray scattering (WAXS)

SAXS and WAXS measurements were simultaneously conducted at the National Synchrotron Radiation Research Center (NSRRC), Hsinchu, Taiwan (BL23A beamline).[42] A CMOS flat panel X-ray area detector C9728DK was situated 13.6 cm from

Published on 03 June 2014. Downloaded by National Tsing Hua University on 11/09/2014 09:34:43.

the sample position for WAXS; a Pilatus 1 MF area detector with two sets of sample-to-detector distance d and X-ray wavelength λ, (4.95 m, 1.771 Å) and (1.20 m, 0.886 Å), were used to cover a wide SAXS Q-range. The scattering wave vector Q defined by $(4\pi/\lambda)\sin\theta$ with scattering angle 2θ was calibrated using silver behenate for SAXS and sodalite and silicon powders for WAXS. Samples were sealed in 1 mm cells (X-ray path length) and measured at ambient temperature. All SAXS data were rigorously corrected for electronic noise, sample transmission, background scattering and detector sensitivity, followed by scaling to absolute intensity based on the scattering of a standard sample of high-density polyethylene.

3.3 Analytical form of the SAXS model

The SAXS absolute intensity for a gel with fractal structure consisting of metal (Ca or Mg) silicate hydrate globules immersed in the solvent can be expressed in general as follows:[18]

$$I(Q) = N\langle\overline{P(Q)}\rangle\, S(Q)_c + \text{bkg} \quad (1)$$

N is a pre-factor related to the number density and average total contrast of scattering length density (SLD) of the globules, $S(Q)_c$ is the corrected inter-globule structure factor of the porous gel taking into account the effect of polydispersity, $\langle\overline{P(Q)}\rangle$ denotes the normalized intra-particle structure factor averaged over the distribution of the size and all possible orientations of the globules, and bkg is the constant incoherent background.

3.3.1 Inter-globule structure factor. Here we assume that the size, orientation, and position are all independent[43] and therefore $S(Q)_c$ can be expressed by eqn (2).

$$S(Q)_c = 1 + \beta(Q)\,[S(Q) - 1], \quad (2)$$

where $\beta(Q) = |\langle F(Q)\rangle|^2/\langle|F(Q)|^2\rangle$. $F(Q)$ is the particle form factor and $S(Q)$[29–31]

$$\begin{aligned} S(Q) &= 1 + N_p\int_0^\infty \mathrm{d}r 4\pi r^2 \frac{\sin(Qr)}{Qr} g(r) \\ &= 1 + \frac{1}{(QR_e)^D}\frac{D\Gamma(D-1)\sin[(D-1)\tan^{-1}(Q\xi)]}{\left[1+(Q\xi)^{-2}\right]^{[(D-1)/2]}} \\ &= 1 + \left(\frac{\xi}{R_e}\right)^D \Gamma(D+1)\frac{\sin[(D-1)\tan^{-1}(Q\xi)]}{(D-1)\left[1+(Q\xi)^2\right]^{[(D-1)/2]}(Q\xi)} \end{aligned} \quad (3)$$

with $\Gamma(x)$ being the Gamma function.

The essential parameters of the inter-globular structure factor are the mass fractal dimension, D, the fractal cutoff dimension, ξ, and the equivalent radius, R_e.

3.3.2 Intra-globule structure factor. The normalized intra-particle structure factor, *i.e.* $\langle\overline{P(Q)}\rangle = \langle|F(Q)|^2\rangle$, includes the size and shape information of the globules and therefore is essential to distinguish the difference in the nanostructure of the building block between the C-S-H and M-S-H gels (for the mathematical details reader can refer to the ESI†).

Based on previous studies,[30,31] the structure of the C-S-H globule can be modelled as a disk with layered sub-structure. The size distribution of the C-S-H globules is assumed to come from the "effective" Schultz distribution of the number of repeating layers n of the multilayer disk. The fitting parameters of the intra-particle structure factor of the C-S-H samples are the disk radius, R, the layer thickness of hydration water, L_1, and of hydrated calcium silicate, L_2, the scattering length density (SLD) contrast ratio $\chi = \frac{\rho_1 - \rho_s}{\rho_2 - \rho_s}$ (ρ_1, ρ_2, and ρ_s are SLDs of the inter-layer confined water, interlayer calcium silicate, and solvent, respectively), the average number of repeating layers inside a globule, $\bar{n}$, and the width parameter, Z_n, of the number of layers described by a Schultz distribution. The equivalent radius R_e in $S(Q)$ can be calculated from the geometrical parameters defining the multilayer disk as $R_e = (3\bar{n}R^2L/4)^{(1/3)}$, where $L = L_1 + L_2$ is the total interlayer distance. The total thickness of each disk, t, can be found by $t = nL$.

In the M-S-H cases the high-Q peak characteristic of the interlayer sub-structure, which is the essential feature of the C-S-H samples, is not present (see Fig. 1b). In addition, there is a broad bump in the high-Q part of the SAXS pattern, which is not explained by a disk-like shape of the primary units. As a consequence, fitting M-S-H curves with the previous multilayer disk model results in unphysical values of both L and L_2 distances (see Table S1 in the ESI†). Therefore, we implemented a simple model of polydisperse homogeneous spheres to describe the intra-particle structure factor, assuming the distribution of the sphere radius to follow a Schultz distribution (see ESI† for the mathematical description of $\langle\overline{P(Q)}\rangle$). The essential fitting parameters of the intra-particle structure factor of the M-S-H samples are the average radius of the spheres, $\bar{R}$, and the width parameter of the sphere radius, Z_R, described by a Schultz distribution. The inter-particle structure factor is described again by eqn (2) and (3), which explicitly consider the formation of a mass fractal structure as a result of the aggregation of the primary globules. In the M-S-H case, the equivalent radius R_e in $S(Q)$ is directly given by $\bar{R}$.

Based on the description above, we analysed the mixed sample through a combined model, assuming that the interaction between C-S-H and M-S-H is negligible at the length-scale studied by SAXS (~1–2000 Å). Therefore, we can express the scattering intensity of SAXS as a linear combination of the intensity contributions from both C-S-H and M-S-H components:

$$\begin{aligned} I(Q) = {} & N_{CSH}\langle\overline{P(Q)}\rangle_{CSH} S(Q)_{c,CSH} \\ & + N_{MSH}\langle\overline{P(Q)}\rangle_{MSH} S(Q)_{c,MSH} + \text{bkg}. \end{aligned} \quad (4)$$

3.4 Field emission scanning electron microscopy (FE-SEM)

Field emission scanning electron microscopy (FE-SEM) was conducted with a ΣIGMA microscope (Carl Zeiss). The acceleration potential used was 5 kV with a working distance of about 2 mm. Energy-dispersive X-ray analysis (EDX) was performed using a silicon-drift detector (Oxford Instruments), directly coupled with FE-SEM working at an optimal distance of 8.5 mm with an accelerating voltage of 10 kV.

 This journal is © The Royal Society of Chemistry 2014

Published on 03 June 2014. Downloaded by National Tsing Hua University on 11/09/2014 09:34:43.

4. Conclusions

Unravelling the microstructure of the principal binding phases is the key to improve the formulation of Portland cements and new green MgO-based cements. In this study, we synthesized both CaO-based and MgO-based silicate-hydrate gels and characterized their microstructure using WAXS, SAXS and SEM techniques. We therefore investigated the multiscale structure across a wide length-scale from a few angstroms to several micrometers. At nanoscale, the primary units of C-S-H gels are polydisperse multilayer disks while the M-S-H globules can be modelled as polydisperse spheres. These primary units organize themselves to form fractal structures below the micrometer length-scale. The globules pack more compactly in the fractal of the M-S-H case even though the fractal domain is much smaller. It is noteworthy that the present work is the first in-depth evaluation of the structure of M-S-H and C-S-H/M-S-H gels.[33]

The intrinsic shape difference between the two kinds of globules in C-S-H and M-S-H gels also reflects in their morphology from submicron to micrometer levels as indicated by SEM images. All C-S-H samples studied exhibit leafy or sheet-like objects arranged in a laminar pattern while M-S-H samples display densely packed spherical particles.

Finally, results from WAXS, SAXS, and SEM all suggest that the interaction between the fractal structures of C-S-H and M-S-H is negligible in the blend sample although the domains of both fractals become much smaller. Therefore, increasing the interaction between the C-S-H and M-S-H particles can be a potential way to solve the compatibility issue.

We believe that this study provides valuable information crucial to develop innovative solutions for improving the commonly used CaO-based cements and also for designing new sustainable and eco-friendly MgO-based cements. In particular, understanding the microstructure of main binding phases in CaO- and MgO-based cements may open up a way to enhance their compatibility or even to modify the M-S-H basic unit by converting its structure from globular into disk-like shapes.

Acknowledgements

Research at MIT is supported by DOE grant number DE-FG02-90ER45429. Research at University of Florence has been supported by the Italian Center for Colloid and Nanoscience, CSGI. The authors thank Prof. Sung-Min Choi and Sung-Hwan Lim for their discussions about the small-angle data analysis. Dr Chun-Jen Su is acknowledged for help with WAXS data reduction.

Notes and references

1 E. M. Gartner and D. E. Macphee, *Cem. Concr. Res.*, 2011, **41**, 736–749.
2 J. H. Sharp, D. E. Macphee and E. M. Gartner, *Adv. Cem. Res.*, 2010, **22**, 195–202.
3 R. J. Flatt, N. Roussel and C. R. Cheeseman, *J. Eur. Ceram. Soc.*, 2012, **32**, 2787–2798.
4 According to the cement chemistry notation: M = MgO, C = CaO, S = SiO_2, and H = H_2O.
5 H. M. Jennings, *Cem. Concr. Res.*, 2008, **38**, 275–289.
6 F. Ridi, E. Fratini and P. Baglioni, *J. Colloid Interface Sci.*, 2011, **357**, 255–264.
7 H. F. W. Taylor, *Cement Chemistry*, Thomas Telford Publishing, 2nd edn, 1997.
8 N. Vlasopoulos and C. R. Cheeseman, *Sustain. Constr. Mater. Technol.*, 2007, 287–294.
9 L. J. Vandeperre, M. Liska and A. Al-Tabbaa, *Cem. Concr. Compos.*, 2008, **30**, 706–714.
10 T. Zhang, C. R. Cheeseman and L. J. Vandeperre, *Cem. Concr. Res.*, 2011, **41**, 439–442.
11 L. J. Vandeperre, M. Liska and A. Al-Tabbaa, *J. Mater. Civ. Eng.*, 2008, **20**, 375–383.
12 K. S. Lackner, *Science*, 2003, **300**, 1677–1678.
13 TR10: Green Concrete - MIT Technology Review (2010), http://www2.technologyreview.com/article/418542/tr10-green-concrete/ accessed March 2014.
14 C. Unluer and A. Al-Tabbaa, *Cem. Concr. Res.*, 2013, **54**, 87–97.
15 L. Mo and D. K. Panesar, *Cem. Concr. Res.*, 2012, **42**, 769–777.
16 H. M. Jennings and J. W. Bullard, *Cem. Concr. Res.*, 2011, **41**, 727–735.
17 A. Bouguerra, A. Ledhem, F. de Barquin, R. M. Dheilly and M. Quéneudec, *Cem. Concr. Res.*, 1998, **28**, 1179–1190.
18 J. Teixeira, in *Structure and Dynamics of Strongly Interacting Colloids and Supramolecular Aggregates in Solution NATO ASI Series Volume 369*, ed. S.-H. Chen, J. S. Huang and P. Tartaglia, Springer, Netherlands, Dordrecht, 1992, pp. 635–658.
19 D. N. Winslow and S. Diamond, *J. Am. Ceram. Soc.*, 1974, **57**, 193–197.
20 J. J. Völkl, R. E. Beddoe and M. J. Setzer, *Cem. Concr. Res.*, 1987, **17**, 81–88.
21 R. E. Beddoe and K. Lang, *Cem. Concr. Res.*, 1994, **24**, 605–612.
22 D. Winslow, J. M. Bukowski and J. F. Young, *Cem. Concr. Res.*, 1995, **25**, 147–156.
23 D. R. Vollet and A. F. Craievich, *J. Phys. Chem. B*, 2000, **104**, 12143–12148.
24 A. J. Allen, C. G. Windsor, V. Rainey, D. Pearson, D. D. Double and N. M. Alford, *J. Phys. D: Appl. Phys.*, 1982, **15**, 1817–1834.
25 J. J. Thomas, H. M. Jennings and A. J. Allen, *Cem. Concr. Res.*, 1998, **28**, 897–905.
26 A. J. Allen, R. C. Oberthur, D. Pearson, P. Schofield and C. R. Wilding, *Philos. Mag. B*, 1987, **56**, 263–288.
27 J. J. Thomas, A. J. Allen and H. M. Jennings, *J. Am. Ceram. Soc.*, 2008, **91**, 3362–3369.
28 J. J. Thomas, A. J. Allen and H. M. Jennings, *J. Phys. Chem. C*, 2009, **113**, 19836–19844.
29 A. J. Allen, J. J. Thomas and H. M. Jennings, *Nat. Mater.*, 2007, **6**, 311–316.
30 W.-S. Chiang, E. Fratini, P. Baglioni, D. Liu and S.-H. Chen, *J. Phys. Chem. C*, 2012, **116**, 5055–5061.
31 W.-S. Chiang, E. Fratini, F. Ridi, S.-H. Lim, Y.-Q. Yeh, P. Baglioni, S.-M. Choi, U-S. Jeng and S.-H. Chen, *J. Colloid Interface Sci.*, 2013, **398**, 67–73.

Published on 03 June 2014. Downloaded by National Tsing Hua University on 11/09/2014 09:34:43.

32 E. Cappelletto, S. Borsacchi, M. Geppi, F. Ridi, E. Fratini and P. Baglioni, *J. Phys. Chem. C*, 2013, **117**, 22947–22953.
33 D. R. M. Brew and F. P. Glasser, *Cem. Concr. Res.*, 2005, **35**, 85–98.
34 I. G. Richardson, *Cem. Concr. Res.*, 2008, **38**, 137–158.
35 F. Pelisser, P. J. P. Gleize and A. Mikowski, *J. Phys. Chem. C*, 2012, **116**, 17219–17227.
36 Y. He, X. Zhao, L. Lu, L. J. Struble and S. Hu, *J. Wuhan Univ. Technol., Mater. Sci. Ed.*, 2011, **26**, 770–773.
37 J. Pourchez, B. Ruot, J. Debayle, E. Pourchez and P. Grosseau, *Cem. Concr. Res.*, 2010, **40**, 242–252.
38 P. J. McDonald, V. Rodin and A. Valori, *Cem. Concr. Res.*, 2010, **40**, 1656–1663.
39 E. Masoero, E. Del Gado, R. J.-M. Pellenq, F.-J. Ulm and S. Yip, *Phys. Rev. Lett.*, 2012, **109**, 155503.
40 G.-C. Cho, J. Dodds and J. C. Santamarina, *J. Geotech. Geoenviron. Eng.*, 2006, **132**, 591–602.
41 A. Sanna, X. Wang, A. Lacinska, M. T. Styles, T. Paulson and M. M. Maroto-Valer, *Miner. Eng.*, 2013, **49**, 135–144.
42 U-S. Jeng, C. H. Su, C.-J. Su, K.-F. Liao, W.-T. Chuang, Y.-H. Lai, J.-W. Chang, Y.-J. Chen, Y.-S. Huang, M.-T. Lee, K.-L. Yu, J.-M. Lin, D.-G. Liu, C.-F. Chang, C.-Y. Liu, C.-H. Chang and K. S. Liang, *J. Appl. Crystallogr.*, 2010, **43**, 110–121.
43 M. Kotlarchyk and S.-H. Chen, *J. Chem. Phys.*, 1983, **79**, 2461.

This journal is © The Royal Society of Chemistry 2014